

PUREPath-B: A Tessellated Bayesian Model for Recovering CMB B-modes over Large Angular Scales of the Sky

VIPIN SUDEVAN¹ AND PISIN CHEN^{1,2,3,4}

¹*Leung Center for Cosmology and Particle Astrophysics, National Taiwan University, Taipei 10617, Taiwan*

²*Department of Physics and Center for Theoretical Sciences, National Taiwan University, Taipei 10617, Taiwan*

³*Graduate Institute of Astrophysics, National Taiwan University, Taipei 10617, Taiwan*

⁴*Kavli Institute for Particle Astrophysics and Cosmology, SLAC National Accelerator Laboratory, Stanford University, Stanford, California 94305, USA*

ABSTRACT

We introduce a comprehensive, custom-developed neural network, the PUREPath-B, that yields a posterior predictive distribution of Cosmic Microwave Background (CMB) B-mode signal conditioned on the foreground contaminated CMB data and informed by the training dataset. Our network employs nested probabilistic multi-modal U-Net framework, enhanced with probabilistic ResNets at skip connections and seamlessly integrates Bayesian statistics and variational methods to minimize the foreground and noise contaminations. During training, the initial prior distribution over network parameters evolves into approximate posterior distributions through Bayesian inference, constrained by the training data. From the approximate joint full posterior of the model parameters, our network infers a predictive CMB posterior during inference and yields summary statistics such as predictive mean, variance of the cleaned map. The predictive standard deviation provides an interpretable measure of per-pixel uncertainty in the predicted mean CMB map. For loss function, we use a linear combination of KL-Divergence loss and weighted MAE—which ensures that maps with higher amplitudes do not dominate the loss disproportionately. Furthermore, the results from the cosmological parameter estimation using the cleaned B-mode power spectrum, along with its error estimates demonstrates our network minimizes the foreground contaminations effectively, enabling accurate recovery of tensor-to-scalar ratio and lensing amplitude.

Keywords: cosmic background radiation — cosmology: observations — diffuse radiation: Deep Learning — Bayesian Neural Network, Variational Inference

1. INTRODUCTION

The CMB serves as a cornerstone for understanding the origin and evolution of the universe, offering precise insights into the initial conditions, composition, and evolution of the universe (Aghanim et al. 2020). Among its polarization components, the B-modes, which are exclusively sourced by tensor perturbations (Seljak & Zaldarriaga 1997; Kamionkowski et al. 1997a,b), offers a unique probe for the primordial gravitational waves, the amplified quantum fluctuations of the gravitational field (Fabbri & Pollock 1983; Mukhanov et al. 1992; Grishchuk 1977) during the inflationary epoch (Guth 1981; Starobinsky 1979). The amplitude of B-modes, quantified by the tensor-to-scalar ratio r , encodes information about the energy scale of inflation, potentially reaching energy levels inaccessible to modern particle accelerators. Therefore, detecting B-modes provides a unique opportunity to test the inflationary paradigm and explore quantum gravitational effects at unprecedented energy scales.

However, accurately estimating B-modes is a significant challenge due to their faintness as compared to astrophysical foreground emissions, instrumental noise, etc. Polarized

emissions from galactic synchrotron radiation, thermal dust, etc., as well as lensing-induced B-modes from large-scale structures, and detector noise dominates the observed signal. A robust detection of B-mode signal requires advanced component separation techniques, extreme instrument sensitivity, control over systematic errors and precise and sensitive measurements over a wide range of angular scales and frequencies. Ongoing and future CMB experiments (Challinor et al. 2018; Allys et al. 2023; Adak et al. 2022; Li et al. 2019; Hui et al. 2018; Abazajian et al. 2022), aim to achieve the sensitivity and frequency range required to isolate primordial B-modes from contaminants.

Recent decades, several foreground minimization and component separation methods (Eriksen et al. 2008b,a; Land & Magueijo 2006; Jaffe et al. 2006; Bennett et al. 2003; Eriksen et al. 2004; Tegmark et al. 2003; Delabrouille et al. 2009; Sudevan et al. 2017; Sudevan & Saha 2020, 2018; Taylor et al. 2006; Hurier et al. 2013) are developed to minimize the effects of foreground contaminations and thereby providing cleaned CMB maps. With the remarkable achievements in the field of machine learning (ML) (Samuel 1959) in tack-

ling various complex real-world challenges, ML based techniques are investigated to minimize the foregrounds in CMB data (Petroff et al. 2020; Wang et al. 2022; Casas et al. 2022; Yan et al. 2023; Yan et al. 2025; Pal et al. 2024; Sudevan & Chen 2024; Defferrard et al. 2020). Some of the other interesting applications of ML in CMB are Farsian et al. (2020); Pal & Saha (2023); Pal et al. (2024); Adams et al. (2023); Petroff et al. (2020); Lambaga et al. (2025); Melsen et al. (2024) and others. In conventional ML framework, a model is trained to understand the relationship between inputs and outputs by fixing the model parameters (ω), the weights and biases. Probabilistic neural networks (Specht 1990) like Bayesian neural networks are developed to address a crucial shortcoming of the standard deep neural networks by incorporating uncertainty considerations in both model and data.

We present a Bayesian network, PUREPath-B, which utilizes probabilistic layers in order to capture the uncertainty over weights by incorporating prior knowledge of the parameters and propagating it through the network to model the prediction uncertainty. Our network, designed to minimize foregrounds in the simulated CMB **B**-mode maps, is best characterised as a tessellated Probabilistic, nested framework composed of n_{reg} (total numebr of regions) probabilistic U-Nets (Ronneberger et al. 2015). Each U-Net consists of n_{map} (total number of maps at different frequencies) encoders to facilitate a multi-modal learning, a latent space, and a decoder with probabilistic ResNets (He et al. 2015) in the **Expanding pathway** of each decoders at skip connections and an output defined by a diagonal multivariate normal distribution.

2. FORMALISM

In a Bayesian network, the model parameters (ω) are stochastic and are sampled from respective posterior distributions $P(\omega|\mathcal{D})$, where, \mathcal{D} is the training dataset with N simulated sets of foreground contaminated CMB maps $\mathbf{X}_j = \{\mathbf{x}_{i,j}\}_{i=1}^n$ at n frequencies as inputs, and N output \mathbf{y}_j (the simulated CMB map for each set j) i.e., $\mathcal{D} = \left\{ \{\mathbf{x}_{i,j}\}_{i=1}^n, \mathbf{y}_j \right\}_{j=1}^N$. For a given prior $P(\omega)$ and \mathcal{D} , the posterior $P(\omega|\mathcal{D})$ (Graves 2011) is updated using the Bayes' principle as follows:

$$P(\omega|\mathcal{D}) = \frac{P(\mathcal{D}|\omega)P(\omega)}{P(\mathcal{D})}. \quad (1)$$

$P(\mathcal{D}|\omega) = \prod_{i=1}^N P(\mathbf{y}_i|\mathbf{X}_i, \omega)$ is the *likelihood* of the observing \mathbf{y}_i for a given \mathbf{X}_i and ω . Estimating exact $P(\omega|\mathcal{D})$ using Bayesian inference (Tipping 2004) is not practical due to the integral over all feasible ω , hence approximate methods like Monte Carlo, Variational Inference (VI) (Kingma & Welling 2013; Hoffman et al. 2013; Knowles 2015) are used. VI approximates exact distribution with a tractable surrogate or varaitonal distribution $Q_\theta(\omega)$ with parameters

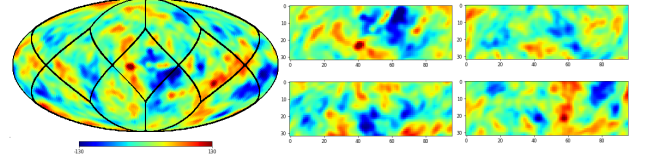


Figure 1. A simulated CMB map is displayed in the left panel in HealPix Mollweide projection. The map is divided with solid black lines into 12 equal area regions with dimension $N_{\text{side}} \times N_{\text{side}}$. Each low-latitude region is stitched together with 2 neighboring higher-latitude areas to form 4 independent plane images of dimension $N_{\text{side}} \times 3N_{\text{side}}$ displayed in the middle and right panel.

θ , optimized to minimize the Kullback-Leibler (KL) divergence $\mathbb{D}_{KL}(Q_\theta(\omega)||P(\omega|\mathcal{D}))$ (Kullback & Leibler 1951),

$$\mathbb{D}_{KL}(Q_\theta(\omega)||P(\omega|\mathcal{D})) = \mathbb{E}_Q[\log Q_\theta(\omega)] - \mathbb{E}_Q[\log P(\omega|\mathcal{D})] + \log(P(\mathcal{D})). \quad (2)$$

In this work, we minimize

$$\mathbb{L} = \frac{1}{N} \sum_i w_i |\mathbf{y}_i^{\text{true}} - \bar{\mathbf{y}}_i^{\text{pred}}| + \beta \mathbb{D}_{KL}(Q_\theta(\omega)||P(\omega|\mathcal{D})), \quad (3)$$

where, $w_i = \frac{1}{A_i + \epsilon} \bigg/ \frac{1}{N} \sum_j \frac{1}{A_j + \epsilon}$ and $A_i = \sqrt{\frac{1}{N_{\text{pix}}} \sum_{j=1}^{N_{\text{pix}}} (\mathbf{y}_{ij}^{\text{true}})^2}$. ϵ is a small constant (10^{-6}) and $\bar{\mathbf{y}}_i^{\text{true}}$ is the target CMB map with N_{pix} number of pixels while β is a tunable hyper parameter to weight the KL-Divergence. The weighted MAE prevents the loss from being dominated by high-amplitude maps, since we use B-mode maps with r -value ranging from 10^{-4} to 10^{-2} . During training, the loss function, \mathbb{L} , is minimized to find the optimal values of θ of the weight distributions. The optimization relies on the Flipout technique (Wen et al. 2018), which provides efficient and low-variance weight perturbations, ensuring stable and effective training.

Once trained, the predictive CMB posterior $\hat{P}(\mathbf{y}^*|\mathbf{X}^*, \mathcal{D})$ of the predicted cleaned CMB map (\mathbf{y}^*) conditioned on \mathbf{X}^* and \mathcal{D} , is estimated using the variational posterior $Q_\theta(\omega|\theta^*)$ of the model parameters as follows,

$$\hat{P}(\mathbf{y}^*|\mathbf{X}^*, \mathcal{D}) \approx \int \hat{P}(\mathbf{y}^*|\mathbf{X}^*, \omega) Q_\theta(\omega|\theta^*) d\omega. \quad (4)$$

This integral can be performed numerically,

$$\hat{P}(\mathbf{y}^*|\mathbf{X}^*, \mathcal{D}) \approx \frac{1}{S} \sum_{s=1}^S \hat{P}(\mathbf{y}^*|\mathbf{X}^*, \omega^s), \quad (5)$$

where, $\hat{P}(\mathbf{y}^*|\mathbf{X}^*, \omega^s) = \mathcal{N}(\mathbf{y}^*|\mu_{\text{CMB}}(\mathbf{x}^*, \omega^s), \sigma_{\text{CMB}}(\mathbf{x}^*, \omega^s))$ (Abdar et al. 2021) is a predictive distribution corresponding to ω^s sampled from $Q_\theta(\omega|\theta^*)$ i.e., $\omega^s \sim Q_\theta(\omega|\theta^*)$. s and S represents the index of the sampling step and the total number of MC samplings respectively, while, μ_{CMB} and σ_{CMB} are the

sample mean and standard deviation estimated from the samples generated in the step s . Using $\hat{P}(\mathbf{y}^*|\mathbf{x}^*, \mathcal{D})$, we compute the summary statistics such as the predictive mean, variance and standard deviation as follows:

$$\mathbb{E}[\mathbf{y}^*|\mathbf{x}^*, \mathcal{D}] \approx \frac{1}{S} \sum_{s=1}^S \mu_{\text{CMB}}^s, \quad (6)$$

$$\text{Var}[\mathbf{y}^*|\mathbf{x}^*, \mathcal{D}] \approx \frac{1}{S} \sum_{s=1}^S \left((\mu_{\text{CMB}}^s - \mathbb{E}[\mathbf{y}^*])^2 + (\sigma_{\text{CMB}}^s)^2 \right), \quad (7)$$

$$\sigma[\mathbf{y}^*|\mathbf{x}^*, \mathcal{D}] = \sqrt{\text{Var}[\mathbf{y}^*|\mathbf{x}^*, \mathcal{D}]}. \quad (8)$$

3. NETWORK ARCHITECTURE

The PUREPath-B architecture, displayed in Figure 2, is a nested combination of multiple U-Nets to handle images from multiple regions in the sky. Each U-Net in turn comprises of as many encoders as the number of input frequency maps. Our network consists of Tensorflow Probability (Abadi et al. 2015) Convolution2DFlipout layers with kernel size 3×3 and strides set as 1 as the feature extracting layers, followed by *parametric*-RELU (p -RELU) activation and LayerNormalization. The Convolution2DFlipout layers are initialized with hierarchical priors that specify a multivariate normal distribution for the layer's weights, allowing the mean and variance to be learned from the data along with mean-field normal posteriors, both provided by Tensorflow. At each encoder layer, the generated feature maps are first concatenated with input maps to that layer and then downsampled using Tensorflow AveragePooling2D. The feature maps from final layer of all encoders in a multi-modal U-Net are combined to form a high-dimensional, abstract representation of inputs images in latent space. These are passed to decoder along with the encoder outputs to form skip-connections. In the decoder, each layer's input consists of upsampled output from the previous decoder layer, the corresponding encoder output at same resolution. Each skip connection incorporates a ResNet Block, which consists of two convolution operations each followed by p -RELU activation and LayerNormalization. A residual connection is formed by adding back the input and this process is repeated 3 times. At the final layer, the decoder outputs are combined and flattened to parameterize a MultivariateNormal-Diag' layer, defining a probabilistic output distribution. The mean represents the network prediction, and the standard deviation quantifies the aleatoric uncertainty.

4. METHODOLOGY

We train our network using foreground-contaminated CMB maps simulated at several LiteBIRD (Allys et al. 2023) frequency channels using software packages CAMB (Lewis & Challinor 2011), HealPix (Górski et al. 2005), and PySM Thorne et al. (2017). The full-sky CMB simulations

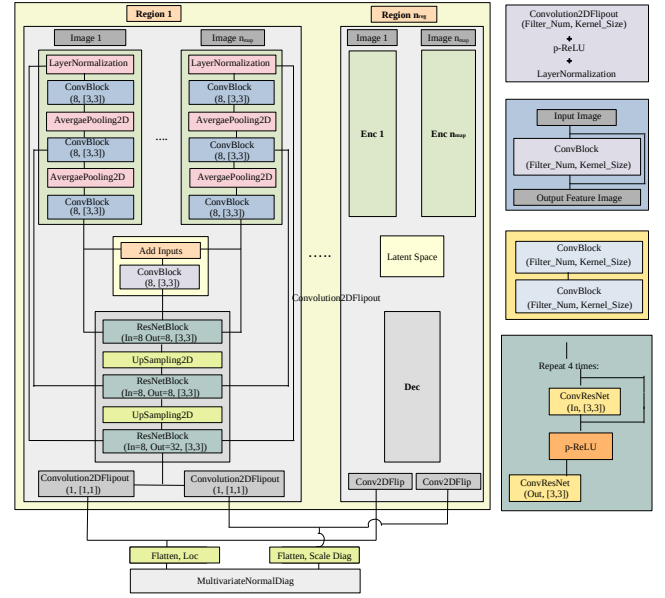


Figure 2. A pictorial representation of our PUREPath-B Model. Input maps corresponding to each region is processed by its own multi-encoder-latent-decoder units. Each encoder block in turn has separate encoder units to process each input map in that region merging into a single latent space and a decoder unit. All the feature maps from the decoders forms the input to a MultivariateNormal-Diag layer, which is the output layer of our model.

follow the Λ -cold dark matter framework by sampling the tensor-to-scale ratio r uniformly between $\log_{10}(0.0001)$ and $\log_{10}(0.05)$ and the Lensing Amplitude A_L from a Gaussian distribution with mean value set at 1.0 and 1% standard deviation while other cosmological parameters are fixed with values provided by Aghanim et al. (2020). Employing CAMB, we generate 3000 lensed CMB B-mode power spectra and the full-sky map using PySM.

Foreground emission maps are simulated using PySM at the eight LiteBIRD frequencies—40, 78, 100, 140, 195, 280, 337 and 402 GHz. For each simulation, we randomly select one model for thermal dust from the set $\{d0, d4\}$, similarly one for synchrotron emission from $\{s1, s2\}$, and one for AME from $\{a1, a2\}$. Consequently, the 3000 foreground simulations are generated from random 8 unique combinations of these foreground models. This ensures our network is trained on a wide array of complex and realistic foreground scenarios, closely mirroring the intricate true sky distribution. Additionally, we generate 3000 noise realizations consistent with the noise model for LiteBird detectors (Allys et al. 2023). All the maps are generated at HealPix $N_{\text{side}} = 32$ with a Gaussian smoothing of FWHM 1.83° .

To ensure seamless integration of Convolution2DFlipout layers, we transform the spherical full-sky maps to approximate plane images (Wang et al. 2022) by reordering all the maps from native HealPix Ring to Nested pixellation. We di-

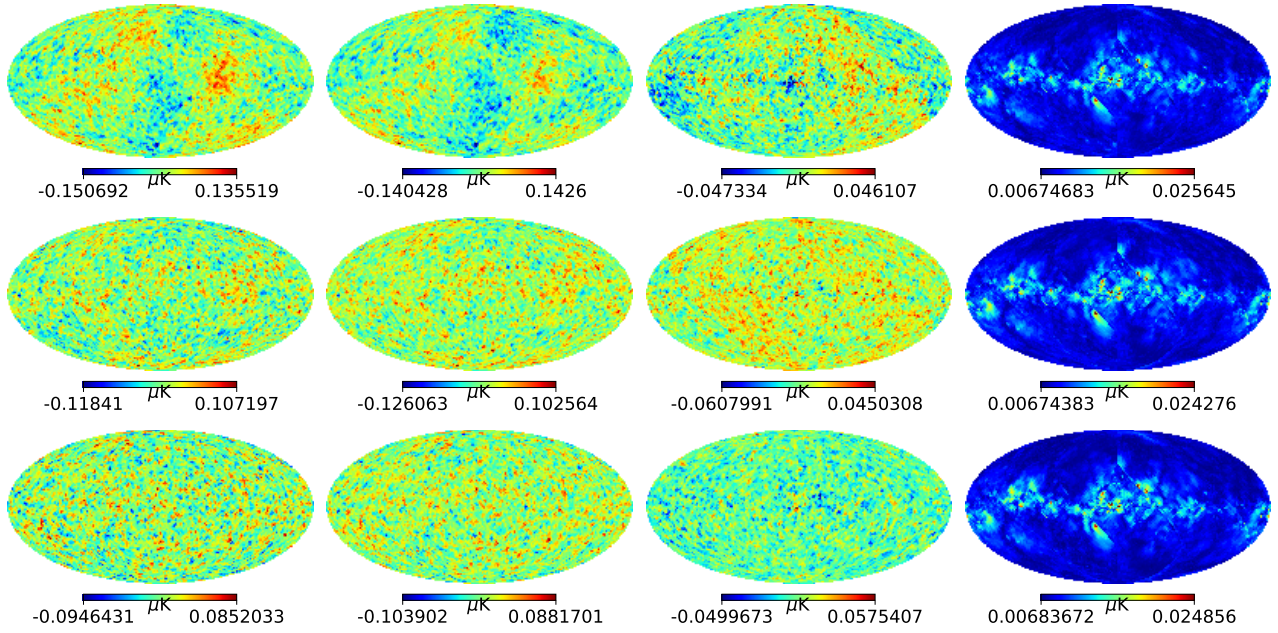


Figure 3. Summary of the performance of our network in minimizing foregrounds at three different r -values. In each row, the left-most panel displays the target CMB map, while the adjacent left-middle panels shows the `Mean_CMap` predicted by our network after minimizing the foregrounds present in the input maps at HealPix $N_{\text{side}} = 32$ and with a 1° beam smoothing. The difference between our `Mean_CMap` and the target CMB maps are shown in the right-middle panels. In the right-most panels, we show the error maps which combines both aleatoric and epistemic uncertainties. The top row corresponds to the results for r -value $= 1.21 \times 10^{-2}$, while middle and bottom row corresponds to results from r -values 4.45×10^{-3} and 6.45×10^{-4} , respectively.

vide the resulting Nested maps to 12 equal area regions with dimension $(N_{\text{side}} \times N_{\text{side}})$ as shown in the left panel of Figure 1 during preprocessing. We take one low-latitude region and combine it with 2 neighboring higher-latitude areas to form 4 independent $(N_{\text{side}} \times 3N_{\text{side}})$ planar maps (Sudevan & Chen 2024). This procedure yields 4 sets of 3000 planar images for each frequency channel. The target full-sky CMB maps are normalized by subtracting the overall mean and dividing by overall standard deviation. We use 2900 samples for training, remaining 100 for testing, and 10% of the training dataset for validation.

Training utilizes a random 80% of the training data in batches of 16 samples every epoch, vastly reducing the memory consumption and improving generalization. The Adam optimizer (Kingma & Ba 2014) is initialized with learning rate 0.01 which is gradually reduced by 25% if validation loss stagnates for 100 epochs. We use Gradient tape for training with gradient accumulation every 5 steps and the network stops training if the validation loss fails to improve over a consecutive 300 epochs. The model weights (mean and standard deviation) corresponding to the lowest validation loss are saved.

5. RESULTS

During inference, for each set of input foreground-contaminated CMB B-mode maps, we repeatedly sample our PUREPath-B's weights to obtain an output distribu-

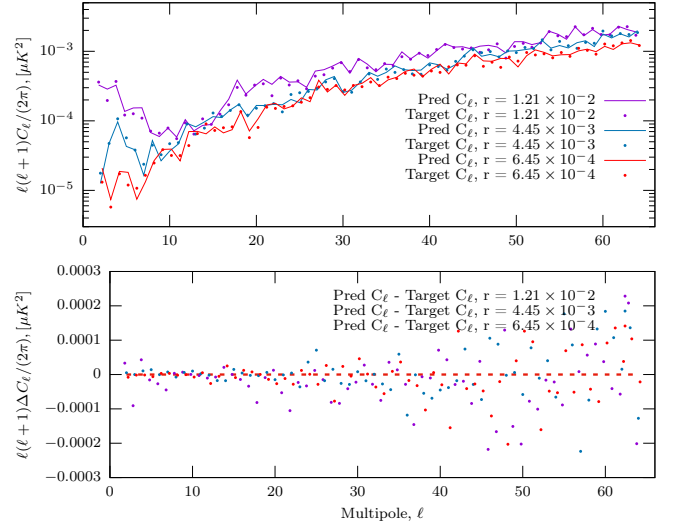


Figure 4. The angular power spectrum estimated from the `Mean_CMap` for r -values 1.21×10^{-2} , 4.45×10^{-3} and 6.45×10^{-4} are shown in violet, blue and red lines respectively. The corresponding target map power spectra is shown in violet, blue and red points. We see excellent agreement between the predicted and target power spectra for all ranges of r at all multipoles. The difference between input and predicted power spectra is shown in the bottom panel.

tion for the cleaned CMB B-mode map. For each weight sample, we extract the sample mean and standard deviation from the corresponding distribution. The final cleaned

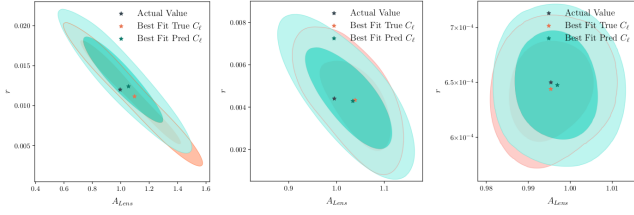


Figure 5. The likelihood estimated using the map power spectrum after taking into account of the network uncertainty is shown in Fig. 4 for r -values 1.21×10^{-2} , 4.45×10^{-3} and 6.45×10^{-4} are displayed in the left, middle and right panels respectively in blue contours. The red contours corresponds to the likelihood estimated using the target map power spectra without including network error. We see that the best-fit value is close to the true value shown as black point.

map (Mean_CMap) is the ensemble mean of these sampled means, while the overall error estimate combines the network's predicted uncertainties (the standard deviation maps from each weight samples) with the dispersion across the sampled means, as described in Eqn. 8. This captures both epistemic and aleatoric contributions. We show results from inference for some representative random r values ($r = 0.012, 0.0045, 0.00065$) in Figure 3, arranged from top to bottom in decreasing order of r . In the left-most panel we show the target CMB B-mode map and the corresponding Mean_CMap predicted by our network in the middle left panel. In the middle right panel we show the difference between the predicted Mean_CMaps and the input CMB maps. From the difference maps we see that our network predictions agree well with the input CMB B-mode maps. In right-most panel we show the error map which captures both epistemic and aleatoric contributions.

The full-sky power spectra of the Mean_CMaps and the input CMB B-mode maps are estimated after properly accounting for the beam and pixel window functions. However, we observe some residual noise bias in our estimated power spectra C_ℓ^{pred} . To correct this bias, we use 80 samples from the testing data and compute for each multipole ℓ the ratio $R(\ell) = C_\ell^{\text{true}} / C_\ell^{\text{pred}}$. For each sample, we fit a linear model $R(\ell) \sim m(\ell)A + c(\ell)$ where A is the mean of C_ℓ^{pred} from $\ell = 2$ to 10. Then for any new predicted spectrum with amplitude A' , the corrected power spectrum is obtained as

$$C_\ell^{\text{correct}} = [m(\ell)A' + c(\ell)]C_\ell^{\text{pred}}. \quad (9)$$

Since this correction is multiplicative, we propagate the uncertainty by applying the same factor to the error estimates (i.e., $\sigma_{C_\ell}^{\text{correct}} = [m(\ell)A' + c(\ell)]\sigma_{C_\ell}^{\text{pred}}$). The corrected power spectra shown in Figure 4 with solid lines representing the power spectra corresponding to Mean_CMaps shown in Figure 3 with violet, green and red colors for r values 0.012, 0.0044, 0.00064 respectively, alongside the corresponding input CMB B-mode maps power spectra in points

with matching colors. We see that estimated power spectra matches well with the input CMB power spectra at all multipoles, ℓ and do not show any signs of bias due to residual foreground or noise contributions. We show the difference between these power spectra in the bottom panel of Figure 4.

We use corrected CMB B-mode map power spectrum to constrain the primordial r -value and lensing amplitude A_{Lens} through cosmological parameter estimation implemented with Cobaya. We use a likelihood function, $L(r, A)$ which is computed as the product of contributions from individual multipoles:

$$L(r, A) = \prod_{\ell=\ell_{\min}}^{\ell_{\max}} L_\ell(r, A). \quad (10)$$

$L(r, A)$ accounts for uncertainty due to cosmic variance and error estimated using our network ($\sigma_{\text{Net}, \ell}^2$). To do this we divided $L(r, A)$ into distinct regimes for low ℓ ($\ell < 30$) and high ℓ as follows:

$$L_\ell(r, A) = \begin{cases} \int_{C_{\min}}^{C_{\max}} dC \frac{C^{\alpha_\ell - 1} e^{-C/\theta_\ell}}{\Gamma(\alpha_\ell) \theta_\ell^{\alpha_\ell}} \cdot \frac{\exp\left[-\frac{(C_\ell^{\text{pred}} - C)^2}{2\sigma_{\text{Net}, \ell}^2 + \epsilon}\right]}{\sqrt{2\pi(\sigma_{\text{Net}, \ell}^2 + \epsilon)}}, & \text{if } \sigma_{\text{Net}, \ell} \geq T, \\ \frac{C_\ell^{\text{pred} \alpha_\ell - 1} e^{-C_\ell^{\text{pred}}/\theta_\ell}}{\Gamma(\alpha_\ell) \theta_\ell^{\alpha_\ell}}, & \text{if } \sigma_{\text{Net}, \ell} < T, \end{cases} \quad \ell < 30, \quad (11)$$

$$\frac{1}{\sqrt{2\pi\sigma_{\text{total}, \ell}^2}} \exp\left[-\frac{(C_\ell^{\text{pred}} - C_\ell^{\text{theory}})^2}{2\sigma_{\text{total}, \ell}^2}\right], \quad \ell \geq 30,$$

where, $\alpha_\ell = \frac{2\ell+1}{2}$, $\theta_\ell = \frac{2C_\ell^{\text{theory}}}{2\ell+1}$, $T = 0.2\sqrt{\theta_\ell^2 \alpha_\ell}$ and $\sigma_{\text{total}, \ell}^2 = \theta_\ell^2 \alpha_\ell + \sigma_{\text{Net}, \ell}^2$. For low multipoles, $\ell < 30$, we perform an adaptive integration over a grid of C_ℓ values in the range defined by $C_\ell^{\text{pred}} \pm 5\theta_\ell^2 \alpha_\ell$. At every grid point, we calculate the logarithm of both Gamma probability density function which represents the cosmic variance and Gaussian probability density function which takes care of the network error. We keep a threshold for network error, i.e., if network error is less than 20% the cosmic variance at that multipole, then network error will not be considered. This is in order to prevent any numerical instabilities due to very small network error. For multipoles $\ell \geq 30$, we adopt a chi-square likelihood with variance as the quadrature sum of cosmic variance and the network error. The likelihood evaluated following this approach is displayed in Fig. 5 for r -values 0.0121, 0.00445 and 0.000645. The maximum likelihood values of r and A_L is very close to the true value signifying our networks predictions along with the error estimates is a valuable tool in minimizing the foreground and noise in the observed CMB B-mode maps.

6. CONCLUSIONS & DISCUSSIONS

By incorporating Bayesian machine learning techniques in conjunction with U-Net and ResNet architectures, our net-

work PUREPath-B, offers a powerful framework to minimize the foreground contaminations in CMB B-mode maps. The uncertainty estimates provided by our network by leveraging its inherent capability to quantify the uncertainty in its predictions can be directly incorporated into subsequent cosmological analyses like parameter estimation etc.

Our network is trained using 3000 sets of simulated foreground contaminated CMB maps at 8 LiteBIRD frequency channels. We use thermal dust, synchrotron and AME as the major sources of foreground contaminations. During training, the prior distributions over model parameters in our network acts as regularization, especially when the training data is limited or noisy. By utilizing Convolution2DFlipout layers and VI techniques, our network efficiently approximate complex posterior distributions of the model parameters. During inference, we implement the testing dataset to evaluate the performance of our network. We estimate predictive mean cleaned maps and its power spectrum corresponding to different values of r and A_{Lens} . The predictive mean maps matches

quite well with the input CMB B-mode map used in those simulations. The Error map quantifies our model's uncertainty on the predicted cleaned CMB map. This is particularly useful in contexts like using our cleaned map for cosmological parameter estimation and other cosmological analyses where understanding the uncertainty in the predicted map is as crucial as the predictions themselves. We provided a method to include the estimated network error to the parameter estimation pipeline.

Overall, the proposed approach provides a comprehensive solution for minimizing foreground and noise contaminations in CMB B-mode maps, enabling more accurate measurements of cosmological parameters and other cosmological analyses.

7. ACKNOWLEDGMENTS

We use publicly available HEALPix Górski et al. (2005) package (<http://healpix.sourceforge.net>) for the analysis of this work. The network we have developed is based on the libraries provided by Tensorflow and Tensorflow Probability.

REFERENCES

- Abadi, M., Agarwal, A., Barham, P., et al. 2015, TensorFlow: Large-Scale Machine Learning on Heterogeneous Systems. <https://www.tensorflow.org/>
- Abazajian, K., et al. 2022. <https://arxiv.org/abs/2203.08024>
- Abdar, M., Pourpanah, F., Hussain, S., et al. 2021, Information fusion, 76, 243
- Adak, D., Sen, A., Basak, S., et al. 2022, Mon. Not. Roy. Astron. Soc., 514, 3002, doi: [10.1093/mnras/stac1474](https://doi.org/10.1093/mnras/stac1474)
- Adams, J., Lu, S., Gorski, K. M., Rocha, G., & Wagstaff, K. L. 2023. <https://arxiv.org/abs/2302.12378>
- Aghanim, N., et al. 2020, Astron. Astrophys., 641, A6, doi: [10.1051/0004-6361/201833910](https://doi.org/10.1051/0004-6361/201833910)
- Allys, E., et al. 2023, PTEP, 2023, 042F01, doi: [10.1093/ptep/ptac150](https://doi.org/10.1093/ptep/ptac150)
- Bennett, C. L., Hill, R. S., Hinshaw, G., et al. 2003, ApJS, 148, 97, doi: [10.1086/377252](https://doi.org/10.1086/377252)
- Casas, J. M., Bonavera, L., González-Nuevo, J., et al. 2022, Astron. Astrophys., 666, A89, doi: [10.1051/0004-6361/202243450](https://doi.org/10.1051/0004-6361/202243450)
- Challinor, A., et al. 2018, JCAP, 04, 018, doi: [10.1088/1475-7516/2018/04/018](https://doi.org/10.1088/1475-7516/2018/04/018)
- Defferrard, M., Milani, M., Gusset, F., & Perraudin, N. 2020, DeepSphere: a graph-based spherical CNN. <https://arxiv.org/abs/2012.15000>
- Delabrouille, J., Cardoso, J. F., Le Jeune, M., et al. 2009, A&A, 493, 835, doi: [10.1051/0004-6361:200810514](https://doi.org/10.1051/0004-6361:200810514)
- Eriksen, H. K., Banday, A. J., Górski, K. M., & Lilje, P. B. 2004, ApJ, 612, 633, doi: [10.1086/422807](https://doi.org/10.1086/422807)
- Eriksen, H. K., Dickinson, C., Jewell, J. B., et al. 2008a, ApJL, 672, L87, doi: [10.1086/526545](https://doi.org/10.1086/526545)
- Eriksen, H. K., Jewell, J. B., Dickinson, C., et al. 2008b, ApJ, 676, 10, doi: [10.1086/525277](https://doi.org/10.1086/525277)
- Fabbri, R., & Pollock, M. 1983, Physics Letters B, 125, 445, doi: [https://doi.org/10.1016/0370-2693\(83\)91322-9](https://doi.org/10.1016/0370-2693(83)91322-9)
- Farsian, F., Krachmalnicoff, N., & Baccigalupi, C. 2020, JCAP, 07, 017, doi: [10.1088/1475-7516/2020/07/017](https://doi.org/10.1088/1475-7516/2020/07/017)
- Górski, K. M., Hivon, E., Banday, A. J., et al. 2005, Astrophys. J., 622, 759, doi: [10.1086/427976](https://doi.org/10.1086/427976)
- Graves, A. 2011, Advances in neural information processing systems, 24
- Grishchuk, L. P. 1977, Soviet Physics Uspekhi, 20, 319, doi: [10.1070/PU1977v020n04ABEH005327](https://doi.org/10.1070/PU1977v020n04ABEH005327)
- Guth, A. H. 1981, Phys. Rev. D, 23, 347, doi: [10.1103/PhysRevD.23.347](https://doi.org/10.1103/PhysRevD.23.347)
- He, K., Zhang, X., Ren, S., & Sun, J. 2015, arXiv e-prints, arXiv:1512.03385, doi: [10.48550/arXiv.1512.03385](https://doi.org/10.48550/arXiv.1512.03385)
- Hoffman, M. D., Blei, D. M., Wang, C., & Paisley, J. 2013, Journal of Machine Learning Research, 14, 1303. <http://jmlr.org/papers/v14/hoffman13a.html>
- Hui, H., et al. 2018, Proc. SPIE Int. Soc. Opt. Eng., 10708, 1070807, doi: [10.1117/12.2311725](https://doi.org/10.1117/12.2311725)
- Hurier, G., Macías-Pérez, J. F., & Hildebrandt, S. 2013, A&A, 558, A118, doi: [10.1051/0004-6361/201321891](https://doi.org/10.1051/0004-6361/201321891)
- Jaffe, T. R., Banday, A. J., Eriksen, H. K., Gorski, K. M., & Hansen, F. K. 2006, Astrophys. J., 643, 616, doi: [10.1086/501343](https://doi.org/10.1086/501343)

- Kamionkowski, M., Kosowsky, A., & Stebbins, A. 1997a, *Phys. Rev. Lett.*, 78, 2058, doi: [10.1103/PhysRevLett.78.2058](https://doi.org/10.1103/PhysRevLett.78.2058)
- . 1997b, *Phys. Rev. D*, 55, 7368, doi: [10.1103/PhysRevD.55.7368](https://doi.org/10.1103/PhysRevD.55.7368)
- Kingma, D. P., & Ba, J. 2014, arXiv e-prints, arXiv:1412.6980, doi: [10.48550/arXiv.1412.6980](https://doi.org/10.48550/arXiv.1412.6980)
- Kingma, D. P., & Welling, M. 2013, arXiv e-prints, arXiv:1312.6114, doi: [10.48550/arXiv.1312.6114](https://doi.org/10.48550/arXiv.1312.6114)
- Knowles, D. A. 2015, arXiv e-prints, arXiv:1509.01631, doi: [10.48550/arXiv.1509.01631](https://doi.org/10.48550/arXiv.1509.01631)
- Kullback, S., & Leibler, R. A. 1951, *The annals of mathematical statistics*, 22, 79
- Lambaga, R. D., Sudevan, V., & Chen, P. 2025. <https://arxiv.org/abs/2501.06139>
- Land, K., & Magueijo, J. 2006, *Mon. Not. Roy. Astron. Soc.*, 367, 1714, doi: [10.1111/j.1365-2966.2006.10078.x](https://doi.org/10.1111/j.1365-2966.2006.10078.x)
- Lewis, A., & Challinor, A. 2011, *CAMB: Code for Anisotropies in the Microwave Background*, *Astrophysics Source Code Library*, record ascl:1102.026
- Li, H., et al. 2019, *Natl. Sci. Rev.*, 6, 145, doi: [10.1093/nsr/nwy019](https://doi.org/10.1093/nsr/nwy019)
- Melsen, J., Flöss, T., & Meerburg, P. D. 2024. <https://arxiv.org/abs/2412.12377>
- Mukhanov, V., Feldman, H., & Brandenberger, R. 1992, *Physics Reports*, 215, 203, doi: [https://doi.org/10.1016/0370-1573\(92\)90044-Z](https://doi.org/10.1016/0370-1573(92)90044-Z)
- Pal, S., & Saha, R. 2023, *J. Astrophys. Astron.*, 44, 84, doi: [10.1007/s12036-023-09974-4](https://doi.org/10.1007/s12036-023-09974-4)
- Pal, S., Yadav, S. K., Saha, R., & Souradeep, T. 2024. <https://arxiv.org/abs/2404.18100>
- Petroff, M. A., Addison, G. E., Bennett, C. L., & Weiland, J. L. 2020, *Astrophys. J.*, 903, 104, doi: [10.3847/1538-4357/abb9a7](https://doi.org/10.3847/1538-4357/abb9a7)
- Ronneberger, O., Fischer, P., & Brox, T. 2015, arXiv e-prints, arXiv:1505.04597, doi: [10.48550/arXiv.1505.04597](https://doi.org/10.48550/arXiv.1505.04597)
- Samuel, A. L. 1959, *IBM Journal of Research and Development*, 3, 210, doi: [10.1147/rd.33.0210](https://doi.org/10.1147/rd.33.0210)
- Seljak, U., & Zaldarriaga, M. 1997, *Phys. Rev. Lett.*, 78, 2054, doi: [10.1103/PhysRevLett.78.2054](https://doi.org/10.1103/PhysRevLett.78.2054)
- Specht, D. F. 1990, *Neural Networks*, 3, 109, doi: [https://doi.org/10.1016/0893-6080\(90\)90049-Q](https://doi.org/10.1016/0893-6080(90)90049-Q)
- Starobinsky, A. A. 1979, *JETP Lett.*, 30, 682
- Sudevan, V., Aluri, P. K., Yadav, S. K., Saha, R., & Souradeep, T. 2017, *The Astrophysical Journal*, 842, 62
- Sudevan, V., & Chen, P. 2024. <https://arxiv.org/abs/2406.19367>
- Sudevan, V., & Saha, R. 2018, *Astrophys. J.*, 867, 74, doi: [10.3847/1538-4357/aae439](https://doi.org/10.3847/1538-4357/aae439)
- . 2020, *Astrophys. J.*, 897, 30, doi: [10.3847/1538-4357/ab964e](https://doi.org/10.3847/1538-4357/ab964e)
- Taylor, J. F., Ashdown, M. A. J., & Hobson, M. P. 2006, in 41st *Rencontres de Moriond: Workshop on Cosmology: Contents and Structures of the Universe (Hanoi: The Gioi)*, 290–292
- Tegmark, M., de Oliveira-Costa, A., & Hamilton, A. J. 2003, *PhRvD*, 68, 123523, doi: [10.1103/PhysRevD.68.123523](https://doi.org/10.1103/PhysRevD.68.123523)
- Thorne, B., Dunkley, J., Alonso, D., & Naess, S. 2017, *Mon. Not. Roy. Astron. Soc.*, 469, 2821, doi: [10.1093/mnras/stx949](https://doi.org/10.1093/mnras/stx949)
- Tipping, M. E. 2004, *Bayesian Inference: An Introduction to Principles and Practice in Machine Learning*, ed. O. Bousquet, U. von Luxburg, & G. Rätsch (Berlin, Heidelberg: Springer Berlin Heidelberg), 41–62, doi: [10.1007/978-3-540-28650-9_3](https://doi.org/10.1007/978-3-540-28650-9_3)
- Wang, G.-J., Shi, H.-L., Yan, Y.-P., et al. 2022, *Astrophys. J. Supp.*, 260, 13, doi: [10.3847/1538-4365/ac5f4a](https://doi.org/10.3847/1538-4365/ac5f4a)
- Wen, Y., Vicol, P., Ba, J., Tran, D., & Grosse, R. 2018, arXiv e-prints, arXiv:1803.04386, doi: [10.48550/arXiv.1803.04386](https://doi.org/10.48550/arXiv.1803.04386)
- Yan, Y.-P., Li, S.-Y., Liu, Y., Xia, J.-Q., & Li, H. 2025, arXiv e-prints, arXiv:2502.09071, doi: [10.48550/arXiv.2502.09071](https://doi.org/10.48550/arXiv.2502.09071)
- Yan, Y.-P., Wang, G.-J., Li, S.-Y., & Xia, J.-Q. 2023, *Astrophys. J.*, 947, 29, doi: [10.3847/1538-4357/acbf4](https://doi.org/10.3847/1538-4357/acbf4)